

A 4D wave packet study of the CH₃I photodissociation in the A-band. Comparison with femtosecond velocity map imaging experiments

A. García-Vela, R. de Nalda, J. Durá, J. González-Vázquez, and L. Bañares

Citation: *J. Chem. Phys.* **135**, 154306 (2011); doi: 10.1063/1.3650718

View online: <http://dx.doi.org/10.1063/1.3650718>

View Table of Contents: <http://jcp.aip.org/resource/1/JCPSA6/v135/i15>

Published by the [American Institute of Physics](#).

Additional information on *J. Chem. Phys.*

Journal Homepage: <http://jcp.aip.org/>

Journal Information: http://jcp.aip.org/about/about_the_journal

Top downloads: http://jcp.aip.org/features/most_downloaded

Information for Authors: <http://jcp.aip.org/authors>

ADVERTISEMENT



AIP Advances

Special Topic Section:
PHYSICS OF CANCER

Why cancer? Why physics? [View Articles Now](#)

A 4D wave packet study of the CH₃I photodissociation in the A-band. Comparison with femtosecond velocity map imaging experiments

A. García-Vela,^{1,a)} R. de Nalda,² J. Durá,^{3,4,b)} J. González-Vázquez,^{2,3} and L. Bañares^{3,a)}

¹Instituto de Física Fundamental, CSIC, C/ Serrano, 123, 28006 Madrid, Spain

²Instituto de Química Física Rocasolano, CSIC, C/ Serrano, 119, 28006 Madrid, Spain

³Departamento de Química Física I, Facultad de Ciencias Químicas, Universidad Complutense de Madrid, 28040 Madrid, Spain

⁴Instituto de Estructura de la Materia, CSIC, C/ Serrano, 123, 28006 Madrid, Spain

(Received 7 September 2011; accepted 22 September 2011; published online 20 October 2011)

The time-resolved photodissociation dynamics of CH₃I in the A-band has been studied theoretically using a wave packet model including four degrees of freedom, namely the C–I dissociation coordinate, the I–CH₃ bending mode, the CH₃ umbrella mode, and the C–H symmetric stretch mode. Clocking times and final product state distributions of the different dissociation (nonadiabatic) channels yielding spin-orbit ground and excited states of the I fragment and vibrationless and vibrationally excited (symmetric stretch ν_1 and umbrella ν_2 modes) CH₃ fragments have been obtained and compared with the results of femtosecond velocity map imaging experiments. The wave packet calculations are able to reproduce with very good agreement the experimental reaction times for the CH₃(ν_1, ν_2)+I*(²P_{1/2}) dissociation channels with $\nu_1 = 0$ and $\nu_2 = 0, 1, 2$, and also for the channel CH₃($\nu_1 = 0, \nu_2 = 0$)+I(²P_{3/2}). However, the model fails to predict the experimental clocking times for the CH₃(ν_1, ν_2)+I(²P_{3/2}) channels with $(\nu_1, \nu_2) = (0, 1), (0, 2),$ and $(1, 0)$, that is, when the CH₃ fragment produced along with spin-orbit ground state I atoms is vibrationally excited. These results are similar to those previously obtained with a three-dimensional wave packet model, whose validity is discussed in the light of the results of the four-dimensional treatment. Possible explanations for the disagreements found between theory and experiment are also discussed. © 2011 American Institute of Physics. [doi:10.1063/1.3650718]

I. INTRODUCTION

Photolysis of CH₃I in the A-band has been considered as a prototypical photodissociation reaction in polyatomic molecules over the last two decades. Among the reasons for this interest is that this is a relatively small polyatomic system presenting an interesting nonadiabatic dynamics. It is therefore liable to be investigated both experimentally and theoretically (using different methodologies), which has produced a rich variety of studies over the years.^{1–33}

The A-band of CH₃I consists of a broad featureless absorption continuum ranging from 220 to 350 nm with a maximum at about 260 nm.¹ Photodissociation of CH₃I in most of this band takes place upon excitation of the system through a strong parallel transition from the \tilde{X}^1A_1 ground electronic state to the ³Q₀ excited electronic state (correlating with the CH₃(\tilde{X}^2A_2'')+I*(²P_{1/2}) products), which in turn is nonadiabatically coupled to the ¹Q₁ excited state (correlating with the CH₃(\tilde{X}^2A_2'')+I(²P_{3/2}) products). There can also be excitation of the system through a perpendicular radiative transition to the ¹Q₁ and ³Q₁ excited states (also correlating with the CH₃(\tilde{X}^2A_2'')+I(²P_{3/2}) products). These three excited states are essentially repulsive (the ³Q₀ state presents a shallow van der Waals well), leading to direct adiabatic dissociation of CH₃I in the femtosecond regime upon absorption.

The combination of the velocity map imaging technique and femtosecond laser pump-probe schemes has revealed as a powerful tool to study in detail fast dissociation processes and, in particular, it has been widely applied to investigate the time-resolved photodissociation dynamics of CH₃I in the A-band^{27–30} and B-band.^{34,35} In previous femtosecond pump-probe experiments on the CH₃I photodissociation in the A-band with 266 nm excitation,^{27,28} we reported relative times, $\tau = \tau_1 - \tau_2$, for the appearance of photoproducts through the channels CH₃(ν_1, ν_2)+I*(²P_{1/2}) and CH₃(ν_1, ν_2)+I(²P_{3/2}) for $(\nu_1, \nu_2) = (0, 0), (0, 1),$ and $(0, 2)$ (ν_1 and ν_2 are the symmetric stretch and umbrella bending modes of CH₃, respectively), with τ_1 and τ_2 being the appearance times associated with the I*(²P_{1/2}) and I(²P_{3/2}) dissociation channels, respectively. The appearance times were also calculated by means of a reduced dimensionality wave packet model including three degrees of freedom.²⁸ While there was very good, quantitative agreement between the experimental and the theoretical relative appearance time for $(\nu_1, \nu_2) = (0, 0)$, this agreement quickly deteriorated as the ν_2 vibrational excitation of CH₃ increased. Indeed, for $\nu_2 = 0$ the experimental relative reaction times decreased remarkably, while the corresponding theoretical times remained rather similar, increasing slightly. A similar result was found for the I(²P_{3/2})/I*(²P_{1/2}) ratio as a function of ν_2 , which showed a reasonable agreement for the experimental and theoretical values for $\nu_2 = 0$, and an increasing divergence for $\nu_2 > 0$. A possible explanation for these discrepancies was suggested²⁸ in the sense that the reduced

^{a)}Authors to whom correspondence should be addressed. Electronic addresses: garciavela@iff.csic.es and banares@quim.ucm.es.

^{b)}Present address: ICFO- Institute of Photonic Sciences, Barcelona, Spain.

dimensionality model would be missing some couplings between the CH₃ umbrella bending mode and some of the neglected modes (mainly the symmetric stretch mode of the CH₃ group), which would become increasingly important with increasing excitation of the umbrella mode.

In the present work, we have carried out wave packet calculations using a four-dimensional (4D) wave packet model, which includes the symmetric stretch mode of the CH₃ group as the fourth degree of freedom (as compared to the previous three-dimensional model used in Ref. 28), and incorporates explicitly the couplings between this mode and the CH₃ umbrella bending mode. Our main goal here is twofold. On one hand, we intend to check our previously suggested explanation about the failure of the three-dimensional (3D) model, and whether the 4D model is able to reliably predict the experimental data. On the other hand, we pursue to assess the validity and accuracy of the 3D model by comparing its performance to that of the 4D treatment. Experimentally, a tunable UV femtosecond laser pump-probe scheme has been combined with the velocity map imaging technique. Here we report experimental absolute appearance times τ_1 for the CH₃(ν_1, ν_2)+I*(²P_{1/2}) dissociation channels with (ν_1, ν_2) = (0, 0), (0, 1), and (0, 2), and absolute appearance times τ_2 for the channels CH₃(ν_1, ν_2)+I(²P_{3/2}) with (ν_1, ν_2) = (0, 0), (0, 1), (0, 2), and (1, 0). It is the first time that such absolute reaction times are measured and reported in the literature.

The paper is organized in the following way. Section II presents the theoretical approach. In Sec. III, the experimental setup is described. In Sec. IV, the experimental and theoretical results are presented and discussed. Finally, conclusions are given in Sec. V.

II. THEORETICAL DYNAMICAL MODEL

A. Model system and initial state

The model used to represent the CH₃I system considers four degrees of freedom (R, r, α, θ), where the dissociation coordinate R is the distance between I and the CH₃ center-of-mass, r is the symmetric C–H bond distance representing the CH₃ symmetric stretch mode (ν_1), α is the umbrella bending angle of the CH₃ group (ν_2), and θ is the in-plane H₃–C–I bending angle (ν_6) between the C–I axis and the axis perpendicular to the plane containing the three hydrogen atoms (see Fig. 1). Out of the total nine vibrational degrees of freedom of CH₃I, the present model is neglecting five degrees of freedom corresponding to the asymmetric stretch, the asymmetric deformation of the CH₃ group, and the out-of-plane H₃–C–I bending mode described by the dihedral angle between I and the plane containing one C–H bond. Wave packet simulations considering five degrees of freedom, namely the current four modes plus the out-of-plane bending mode, have shown that this latter mode plays a small role in the CH₃I photodissociation dynamics and can be ignored,¹⁴ and this is why it is neglected in the present model. Furthermore, full-dimensional, 9D calculations carried out using the multiconfiguration time-dependent Hartree (MCTDH) scheme have been recently reported,¹⁵ and they show that the 5D and 9D descriptions lead to rather similar results. It is expected, there-

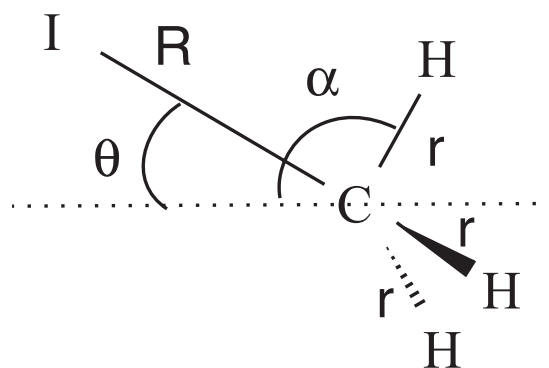


FIG. 1. Coordinates used in the 4D representation.

fore, that the four modes considered in the current model are able to describe reliably the main features of the CH₃I nonadiabatic photodissociation dynamics in the A-band.

In the model, zero total angular momentum ($J = 0$) is assumed for the system, and in this case the four-dimensional nuclear kinetic energy operator can be written as

$$\hat{T} = -\frac{\hbar^2}{2} \left[\frac{1}{\mu} \frac{\partial^2}{\partial R^2} + \left(\frac{1}{3m_H} + \frac{\cos^2 \alpha}{m_C} \right) \frac{\partial^2}{\partial r^2} - \frac{1}{m_C} \left(\frac{1}{r} \frac{\partial}{\partial r} - \frac{1}{r^2} \right) \left(3 \cos^2 \alpha - 1 + 2 \cos \alpha \sin \alpha \frac{\partial}{\partial \alpha} \right) - \frac{1}{\hbar^2} \left(\frac{1}{3m_H r^2} + \frac{\sin^2 \alpha}{m_C r^2} \right) \hat{j}^2 - \frac{1}{\hbar^2} \left(\frac{1}{\mu R^2} + \frac{2}{3m_H r^2 \sin^2 \alpha} \right) \hat{l}^2 + \frac{\cos \alpha \sin \alpha}{m_C r^2} \frac{\partial}{\partial \alpha} \right]. \quad (1)$$

In the above expression, μ is the reduced mass associated with the R mode, $\mu = m_I(m_C + 3m_H)/(m_I + m_C + 3m_H)$, where m_I , m_C , and m_H are the masses of the I, C, and H atoms, respectively, and \hat{j} and \hat{l} are the angular momentum operators associated with the α and θ angles, respectively. The \hat{T} operator of Eq. (1) has been derived from the five-dimensional operator reported in Ref. 14.

At the $\lambda = 267$ nm excitation wavelength used in this work the intensity of the ${}^3Q_1 \leftarrow \tilde{X}^1A_1$ transition is negligible and the intensity of the ${}^1Q_1 \leftarrow \tilde{X}^1A_1$ transition is remarkably smaller than that of the ${}^3Q_0 \leftarrow \tilde{X}^1A_1$ transition. Thus, in the model the ${}^3Q_1 \leftarrow \tilde{X}^1A_1$ transition is neglected and only the ${}^3Q_0 \leftarrow \tilde{X}^1A_1$ and ${}^1Q_1 \leftarrow \tilde{X}^1A_1$ transitions are considered. In previous 3D simulations of the CH₃I photodissociation dynamics,²⁸ only the most intense ${}^3Q_0 \leftarrow \tilde{X}^1A_1$ transition was considered.

The \tilde{X}^1A_1 ground electronic potential surface is represented as a sum of four potential functions

$$V_g(R_{C-I}, r, R_{C-H_3}, \theta) = V_a(R_{C-I}) + V_b(r) + V_c(R_{C-H_3}) + V_d(\theta), \quad (2)$$

where R_{C-I} is the C–I bond distance and R_{C-H_3} is the distance between C and the center-of-mass of the three hydrogen atoms, being $R_{C-H_3} = -r \cos \alpha$. The $V_a(R_{C-I})$

interaction potential is taken from the CH₃I two-dimensional ground-state potential computed through multireference spin-orbit configuration interaction *ab initio* calculations.²⁵ The $V_b(r)$ interaction potential is described by a harmonic oscillator function $V_b(r) = \frac{1}{2}k_b(r - r_0)^2$ with $k_b = 3m_H\omega_b^2$, $\omega_b = 3004 \text{ cm}^{-1}$, and $r_0 = 1.084 a_0$. The remaining $V_c(R_{C-H_3})$ and $V_d(\theta)$ potentials are also represented by harmonic oscillator functions, and they have been described in detail elsewhere.²⁸ The $V_a(R_{C-I})$ and $V_c(R_{C-H_3})$ interaction potentials are transformed to the (R, r, α, θ) coordinates in order to obtain a ground potential surface $V_g(R, r, \alpha, \theta)$.

The excited electronic surfaces 3Q_0 and 1Q_1 , and the nonadiabatic coupling between them are described by the *ab initio* surfaces calculated by Xie *et al.*,²¹ which are an improved version of the previous nine-dimensional surfaces of Amatatsu *et al.*¹⁷ In order to reduce the dimensionality of these surfaces, some of the coordinates are fixed at their equilibrium values. Specifically, the out-of-plane bending angle is set to $\phi = 0$, and the three β angles (one of which is redundant) between the two planes containing C–H bonds are fixed to $\beta_1 = \beta_2 = \beta_3 = 2\pi/3$ (see Fig. 1 of Ref. 17). The transition dipole moment functions μ_{ge} for the $^3Q_0 \leftarrow \tilde{X}^1A_1$ and $^1Q_1 \leftarrow \tilde{X}^1A_1$ transitions are taken from the *ab initio* data of Alekseyev *et al.*,²⁶ which are fitted to functional forms that have been reported earlier.³²

The initial state of CH₃I is calculated variationally on the ground electronic potential surface $V_g(R, r, \alpha, \theta)$ by solving the Schrödinger equation

$$[\hat{T} + V_g(R, r, \alpha, \theta)]\psi(R, r, \alpha, \theta) = E\psi(R, r, \alpha, \theta), \quad (3)$$

where \hat{T} is the operator of Eq. (1). Due to the presence of four coupled degrees of freedom, a rigorous variational solution of the above equation involves an extremely costly diagonalization of a large Hamiltonian matrix. Thus Eq. (3) has been solved by means of a two step procedure. In a first step, the following Schrödinger equation is solved

$$[\hat{T}' + V_b(r) + V_c(r, \alpha)]\varphi_{\nu_1, \nu_2}^{(l)}(r, \alpha) = E_{\nu_1, \nu_2}^{(l)}\varphi_{\nu_1, \nu_2}^{(l)}(r, \alpha), \quad (4)$$

where the operator \hat{T}' includes all the terms of \hat{T} that depend on r and α , that is

$$\hat{T}' = \hat{T} - \left(-\frac{\hbar^2}{2\mu} \frac{\partial^2}{\partial R^2} + \frac{\hat{l}^2}{2\mu R^2} \right).$$

The ν_1 , ν_2 , and l indices are the quantum numbers associated with the r and α modes, and with the \hat{l} operator, respectively. In order to solve Eq. (4), the Hamiltonian matrix is represented in a basis set. Specifically, 4 harmonic oscillator functions (or Hermite functions) are used to represent the r mode, while 50 and 24 Legendre polynomials [$P_j(\cos \alpha)$ and $P_l(\cos \theta)$] are used to represent the α and θ modes, respectively. After diagonalizing the Hamiltonian matrix of Eq. (4) the wave functions $\varphi_{\nu_1, \nu_2}^{(l)}(r, \alpha)$ and energies $E_{\nu_1, \nu_2}^{(l)}$ are obtained, and they are now used as basis functions to represent the full Hamiltonian of Eq. (3) and to solve this equation.

The initial state of our system is the ground vibrational state of CH₃I. That ground state can be obtained by using only the $\varphi_{\nu_1, \nu_2}^{(l)}(r, \alpha)$ basis functions with $\nu_1 = \nu_2 = 0$ and $l = 0 - 23$ in order to represent the Hamiltonian of Eq. (3). There-

fore, in a second step the equation,

$$\left[-\frac{\hbar^2}{2\mu} \frac{\partial^2}{\partial R^2} + \frac{\hat{l}^2}{2\mu R^2} + E_{0,0}^{(l)} + V_a(R, r, \alpha, \theta) + V_d(\theta) \right] \psi(R, r, \alpha, \theta) = E\psi(R, r, \alpha, \theta), \quad (5)$$

is solved by representing the R coordinate in a uniform grid of 101 equidistant points in the range $3.5 a_0 \leq R \leq 6.63 a_0$ using the Fourier grid Hamiltonian method,³⁶ the r and α coordinates by the $\varphi_{0,0}^{(l)}(r, \alpha)$ basis functions, and the θ coordinate by 24 Legendre polynomials $P_l(\cos \theta)$, and then diagonalizing. The lowest eigenfunction obtained from the diagonalization, with an associated eigenenergy $E = -17146.22 \text{ cm}^{-1}$ relative to the asymptote of the ground potential surface is the system initial state.

B. Wave packet simulations

In order to simulate the time-resolved pump-probe experiments reported here, excitation of CH₃I through the $^3Q_0 \leftarrow \tilde{X}^1A_1$ and $^1Q_1 \leftarrow \tilde{X}^1A_1$ transitions is carried out in the wave packet calculations by means of a pump laser pulse which is assumed to have a Gaussian profile

$$A(t) = Ae^{-(t-t_0)^2/2\sigma^2}, \quad (6)$$

being $A = 0.001$, $t_0 = 0$ fs, and $\sigma = 42.5$ fs. Such a pulse spreads over a temporal range of 300 fs (from $t = -150$ to $t = 150$ fs) with a full width at half maximum (FWHM) of 100 fs, which is approximately the width estimated for the pump laser pulses produced and used in the experiments.

For the sake of simplicity, we shall adopt the following notation in the remaining of the paper. The three electronic states \tilde{X}^1A_1 , 3Q_0 , and 1Q_1 involved in the CH₃I photodissociation will be denoted by $|0\rangle$, $|1\rangle$, and $|2\rangle$, respectively, and correspondingly, their associated potential surfaces by \hat{V}_0 , \hat{V}_1 , and \hat{V}_2 . The nonadiabatic coupling between the excited states $|1\rangle$ and $|2\rangle$ will be denoted by \hat{V}_{12} . The state $|0\rangle$ is radiatively coupled to the $|1\rangle$ and $|2\rangle$ states by the couplings $\mu_{01}E(t)$ and $\mu_{02}E(t)$, respectively, where μ_{01} and μ_{02} are the $^3Q_0 \leftarrow \tilde{X}^1A_1$ and $^1Q_1 \leftarrow \tilde{X}^1A_1$ transition moment functions, respectively, and the linearly polarized electric field has the form $E(t) = A(t)\cos \omega_0 t$, with ω_0 being the photon frequency of the incident radiation, which in the present case corresponds to the wavelength $\lambda = 267$ nm.

Now the wave packet can be expressed as

$$\Phi(R, r, \alpha, \theta, \mathbf{Q}, t) = \psi_0(R, r, \alpha, \theta, t)|0\rangle + \psi_1(R, r, \alpha, \theta, t)|1\rangle + \psi_2(R, r, \alpha, \theta, t)|2\rangle, \quad (7)$$

with \mathbf{Q} denoting the electronic coordinates. The time evolution of Φ is governed by the time-dependent Schrödinger equation

$$i\hbar \frac{\partial \Phi}{\partial t} = \hat{\mathbf{H}}\Phi, \quad (8)$$

which can be written in matrix form as

$$i\hbar \begin{pmatrix} \dot{\psi}_0 \\ \dot{\psi}_1 \\ \dot{\psi}_2 \end{pmatrix} = \begin{pmatrix} \hat{H}_0 & \mu_{01}E(t) & \mu_{02}E(t) \\ \mu_{10}E(t) & \hat{H}_1 & \hat{V}_{12} \\ \mu_{20}E(t) & \hat{V}_{21} & \hat{H}_2 \end{pmatrix} \begin{pmatrix} \psi_0 \\ \psi_1 \\ \psi_2 \end{pmatrix}, \quad (9)$$

where $\hat{H}_i = \hat{T} + \hat{V}_i$ [\hat{T} being the operator of Eq. (1)], $\mu_{10} = \mu_{01}$, $\mu_{20} = \mu_{02}$, and $\hat{V}_{12} = \hat{V}_{21}$. The initial conditions of Eq. (9) are $\psi_0(R, r, \alpha, \theta, t = 0) = \psi(R, r, \alpha, \theta)$, $\psi_1(R, r, \alpha, \theta, t = 0) = \psi_2(R, r, \alpha, \theta, t = 0) = 0$.

The wave packet is represented in a basis set consisting of a grid of 400 equidistant points in the R coordinate in the range $3.5 a_0 \leq R \leq 16.0 a_0$, and 4 Hermite functions for the r coordinate, regarding the radial variables. For the angular coordinates, discrete variable representations (DVR) consisting of Gauss-Legendre quadratures of 85 and 45 points for α and θ , respectively, are used in the ranges $0 \leq \alpha, \theta \leq \pi$. The action of the \hat{j}^2 and \hat{l}^2 angular momentum operators on the wave packet is computed by using finite basis representations (FBR) of the α and θ dependence of the wave packet consisting of 50 $P_j(\cos \alpha)$ and 24 $P_l(\cos \theta)$ Legendre polynomials. The wave packet is propagated for 500 fs with a time step $\Delta t = 0.1$ fs, using the Chebychev polynomial expansion method to express the evolution operator. Despite that the time step is relatively small, the Chebychev scheme is found to be quite efficient. The wave packet is absorbed at the edge of the grid in the R coordinate after each propagation time step by multiplying each ψ_i packet by the function $\exp[-\alpha(R - R_{abs})^2]$, with $\alpha = 0.9 a_0^{-2}$ and $R_{abs} = 13.0 a_0$.

C. Calculation of observable magnitudes

Photodissociation of CH_3I occurs through two fragmentation channels, namely $\text{CH}_3(\tilde{X}^2A_2'') + \text{I}^*(^2P_{1/2})$ and $\text{CH}_3(\tilde{X}^2A_2'') + \text{I}(^2P_{3/2})$. For simplicity, from now on the $\text{CH}_3(\tilde{X}^2A_2'')$, $\text{I}^*(^2P_{1/2})$, and $\text{I}(^2P_{3/2})$ fragments will be denoted by CH_3 , I^* , and I , respectively. In the above two channels, the CH_3 fragment is produced in different vibrational and rotational states of the various modes, namely the C–H symmetric stretch mode, the umbrella mode, and the CH_3 rotation. One of the goals of this work is to analyze the populations of those CH_3 fragment states. Such analysis requires the computation of those CH_3 fragment rovibrational eigenstates.

The CH_3 rovibrational eigenstates $\varphi_{v_1, v_2}^{(l)}(r, \alpha) P_l(\cos \theta)$ are calculated by solving an equation similar to Eq. (4) for $\varphi_{v_1, v_2}^{(l)}(r, \alpha)$, namely

$$[\hat{T}' + V_{\text{CH}_3}(r, \alpha)]\varphi_{v_1, v_2}^{(l)}(r, \alpha) = E_{v_1, v_2}^{(l)}\varphi_{v_1, v_2}^{(l)}(r, \alpha), \quad (10)$$

where \hat{T}' is the same kinetic energy operator of Eq. (4), and the indices v_1 , v_2 , and l have been already defined. This equation is solved similarly as described above for Eq. (4). For the V_{CH_3} interaction potential the function reported in Ref. 17 has been used [see Eq. (1) and Table 1 of Ref. 17], with $\beta_1 = \beta_2 = \beta_3 = 2\pi/3$. The only difference between the present CH_3 potential and that of Ref. 17 is that two of the parameters have been slightly modified. Specifically, the parameters $k_{22} = 0.012559$ a.u. and $k_1 = 0.388582$ a.u. of Ref. 17 have

TABLE I. Calculated and experimental frequencies of CH_3 (in cm^{-1}).

Assignment	CH_3	
	Theory	Expt.
2 ₁	605.7	606 ^a
2 ₂	1290.2	1288 ^a
2 ₃	2030.3	2019 ^a
2 ₄	2814.1	2790 ^{a, b}
1 ₁	3004.0	3004 ^c
1 ₁ 2 ₁	3615.4	
2 ₅	3640.1	3600 ^{a, b}
1 ₁ 2 ₂	4315.6	4268 ^d
2 ₆	4486.5	4445 ^{a, b}
1 ₁ 2 ₃	5067.3	
2 ₇	5363.5	5322 ^{a, b}
1 ₁ 2 ₄	5862.3	
1 ₂	6008.2	5960 ^d
2 ₈	6263.7	6229 ^{a, b}
1 ₂ 2 ₁	6633.3	
1 ₁ 2 ₅	6697.9	
2 ₉	7184.2	7163 ^{a, b}
1 ₂ 2 ₂	7342.4	
1 ₁ 2 ₆	7558.8	

^aReference 37.

^bReference 38.

^cReference 39.

^dReference 40.

been modified to $k_{22} = 0.010869$ a.u. and $k_1 = 0.342835$ a.u. in the present CH_3 potential function. By doing this modification in the parameters the calculated frequencies of CH_3 agree better with the experimental ones. In Table I, the first 19 calculated frequencies of CH_3 are shown and compared with those observed experimentally.^{37–40} Agreement is very good in general, particularly for the fundamental frequencies of the umbrella and symmetric stretch modes, 606 and 3004 cm^{-1} , respectively.

Now, population of the CH_3 rovibrational states is calculated as a function of time by projecting out the wave packet onto the corresponding states. Such populations are obtained by means of the method of Balint-Kurti *et al.*,^{41,42}

$$P_{v_1, v_2, l}^{(i)}(E, t) = C v_0 k_{v_1, v_2, l}^{(i)} \left| \int_0^t \langle \varphi_{v_1, v_2}^{(l)}(r, \alpha) P_l(\cos \theta) \times |\psi_i(R_c, r, \alpha, \theta, t')\rangle e^{iEt'/\hbar} dt' \right|^2, \quad (11)$$

where C is a constant factor, $v_0 = \omega_0/2\pi$ is the incident photon frequency (corresponding to $\lambda = 267$ nm), $i = 1, 2$, R_c is a suitably large distance of the dissociation coordinate R , E is the total energy of the system reached with $\lambda = 267$ nm radiation, $E = E_i + \hbar\omega_0$ (being E_i the energy of the CH_3I initial state), and $k_{v_1, v_2, l}^{(i)}$ is given by

$$k_{v_1, v_2, l}^{(i)} = [2\mu(E - \epsilon\delta_{i1} - E_{v_1, v_2}^{(l)})]^{1/2}, \quad (12)$$

being ϵ the spin-orbit splitting between the two electronic states of I and δ_{i1} the Kronecker delta. By summing over the rotational states the population in each vibrational state

(ν_1, ν_2) can be obtained as

$$P_{\nu_1, \nu_2}^{(i)}(E, t) = \sum_l P_{\nu_1, \nu_2, l}^{(i)}(E, t). \quad (13)$$

Excitation of CH₃I with a pump pulse of finite temporal width creates a wave packet with a spectral bandwidth. When measuring the magnitudes of interest, a time-resolved experiment detects contributions from all of the energies E of CH₃I contained in the wave packet spectral bandwidth. Thus, in order to take into account this effect in the simulations, the wave packet is projected out for several hundreds of total energies E (specifically 701 energies) covering the whole energy range of the wave packet bandwidth. The probabilities $P_{\nu_1, \nu_2, l}^{(i)}(E, t)$ obtained for all of these E energies are then averaged over the range of the spectral bandwidth, and an average probability $P_{\nu_1, \nu_2, l}^{(i)}(t)$ is obtained. In this way, the calculated rovibrational populations of the CH₃ fragment are more comparable to those observed experimentally. It is noted that in the previous 3D simulations²⁸ all the magnitudes were calculated at a single CH₃I energy $E = E_i + \hbar\omega_0$, corresponding to the central energy of the pump pulse bandwidth, so the effect of the whole pump pulse bandwidth was not taken into account.

Similarly, the finite temporal width of the probe pulse used in the experiment involves a spectral bandwidth which originates an energy window for experimental detection of the fragments. The experiment can detect CH₃ and I* (I) fragments which are not yet completely separated, and which still interact to some extent with an interaction potential energy within the range covered by half the spectral bandwidth of the probe pulse.²⁸ The effect of this detection energy window is considered in the current simulations in the same manner as in the earlier work.²⁸

We can summarize the current procedure of averaging the calculated time-dependent probabilities over the spectral bandwidth of both the pump and probe pulses in the following way. The $P_{\nu_1, \nu_2, l}^{(i)}(E, t)$ probabilities are calculated at several fixed CH₃-I distances R_c (specifically 33 R_c distances) corresponding to the same number of CH₃-I interaction potential energies within the detection energy window originated by the probe pulse. For each fixed distance R_c , the probabilities are calculated and averaged over the energies of the pump pulse spectral bandwidth as described above. Then the averaged probabilities computed for the different R_c distances, or equivalently the different CH₃-I potential energies ε , are weighted with the probe pulse spectral bandwidth distribution $G(\varepsilon)$, and by averaging over all of the weighted values, final rovibrational probabilities for the CH₃ fragment are obtained.

D. Wave packet simulations with three degrees of freedom

A most interesting point is to determine how different is the description of the CH₃I photodissociation dynamics by the present 4D model in comparison with the previous 3D model,²⁸ and what is gained by adding a fourth degree of freedom like the C-H symmetric stretch mode. To this purpose 3D wave packet simulations using the earlier model (described in detail in Ref. 28) have been carried out. In order to make more comparable the 4D and the 3D simulations, in the

present 3D model it is considered that excitation of CH₃I takes place through both the ${}^3Q_0 \leftarrow \tilde{X}^1A_1$ and ${}^1Q_1 \leftarrow \tilde{X}^1A_1$ transitions, and that the pump laser pulse has a spectral bandwidth over which the calculated quantities are averaged, in the same way as described in Sec. II C for the 4D model. These are the only two differences between the current and the earlier²⁸ 3D treatments. Now, the differences between the 4D and the 3D approaches used here are essentially two, namely the addition of the symmetric stretch mode and the description of the umbrella mode as a true bending mode in the 4D model instead of as a Jacobian stretch mode as done in the 3D model.

III. EXPERIMENT

The femtosecond velocity map imaging experimental setup has been described in detail elsewhere^{28,30} and only those aspects relevant to the present experiments will be presented here. The laser is a chirped-pulse amplification (CPA) Ti:sapphire system delivering 80 fs, 1 mJ pulses centered at 802 nm at 1 kHz repetition rate. The fundamental output is split into two arms in a 80:20 splitter. The weaker beam is frequency tripled in a third-harmonic generation unit and provides the 267 nm pump beam for the experiment. The remaining beam is used to pump an optical parametric amplifier (OPA), where signal and idler pulses are generated in a BBO crystal. The signal pulse is later frequency quadrupled to constitute the probe beam around 325–334 nm to detect CH₃ radicals in different vibrational states (vibrationless $\nu = 0$ at 333.5 nm, and $\nu_2=1$ and $\nu_2=2$ in the ν_2 umbrella mode at 329.4 nm and 325.8 nm, respectively) by 2 + 1 REMPI through the $3p_z$ Rydberg state. The bandwidth of both pump and probe lasers is 3 nm FWHM. A PC-controlled, motorized delay stage in the pump arm provides controllable delay between the two pulses. Typical beam energies on the experiment are around 1 μ J/pulse and 3 μ J/pulse for the pump and probe beams, respectively. The time duration of the pump and probe pulses is estimated to be around 120 fs, limited by the observed cross-correlation of around 200 fs. Independent polarization control in each arm is provided by the use of half-wave plates, and telescopes are used to control their focussing geometry on target. The pump and probe laser beams are propagated into the vacuum chamber collinearly and focused with a 25 cm focal length lens into the interaction region of the chamber. Their polarization is kept parallel to the detector face to provide the cylindrical symmetry required for the procedure of Abel inversion of ion images.

The vacuum chamber is divided into three parts: source, ionization and detection. The molecular beam is generated in the source chamber, which is differentially pumped from the other two. During the experiments, CH₃I is kept in a salt/ice bath. A supersonic molecular pulsed beam of CH₃I seeded in He (1.5 bar) is formed in a 1 kHz piezoelectric homemade valve.⁴³ The lasers are fired in the early part of the gas pulse to avoid the presence of clusters in the molecular beam. The gas pulse passes through a 0.5 mm skimmer that separates the source chamber from the ionization chamber. Once in the ionization chamber, the molecular beam flies between the repeller and the extractor plates of a gridless ion lens electrode system located perpendicularly to it and to the propagation of

the laser beams. The ions created in the interaction region are extracted towards the 60 cm time-of-flight tube at the end of which sits the detector, a dual microchannel plate (MCP) coupled to a phosphor screen. Appropriate voltages to the electrodes are applied so that velocity mapping configuration⁴⁴ is achieved. Optimum velocity mapping conditions were obtained with $V_{\text{extractor}}/V_{\text{repeller}}=0.79$ ($V_{\text{repeller}}=5200$ V). By applying a gated voltage to the front plate of the MCP, a selective detection of ion masses can be achieved. The 2D mass-selected images on the phosphor screen are recorded with a Peltier-cooled 12-bit CCD camera and stored in a PC. The velocity, and thus the kinetic energy, of the ions, was calibrated using the well-known CH_3 images produced in the photodissociation of CH_3I . In these conditions, the kinetic energy resolution of the apparatus is better than 100 meV at 1 eV kinetic energy release.

The methodology in a typical experiment is as follows: the sample, containing both CH_3I molecules and clusters, is excited into the dissociative *A*-band by the 267 nm pump beam. After a varying delay, the resulting neutral CH_3 fragment is ionized in a $2 + 1$ REMPI process by the probe beam. The ions resulting from the process are mass selected and imaged onto the detector, typically using for the camera an exposure time of 10–60 s, i.e. corresponding to the accumulation of some tens of thousands of laser shots. The acquisition and storage process, together with the control of the position of the delay line, is fully PC automatized. The raw images are Abel inverted with the pBasex method⁴⁵ where polar coordinates are applied for the inversion.

In these time-resolved experiments, it is crucial to determine accurately the time zero, defined as the position of temporal overlap between the pump and probe laser pulses on target, in order to measure the absolute reaction times for the different channels of the photodissociation process. We have determined time zero between the pump and probe pulses, and also their cross-correlation function, by the *in situ* measurement of the parent ion transient of *N,N*-diethyl aniline by $1+1'$ REMPI.^{20,27,28} Alternatively, when measuring the CH_3 images by setting the appropriate gated voltage to the front plate of the MCP detector, the parent ions can be also detected in the image. This is achieved by conveniently reducing the voltage of the gate in such a way that the gain of the detector outside the CH_3 fragment detection temporal window is not drastically reduced as to permit the detection of parent ions, which are produced in high amount by $1+1'$ REMPI around the temporal overlap of the pump and probe pulses. By integrating the part of the image which corresponds to the parent ions (these ions appear in the central part of the image and do not interfere with the rings corresponding to the CH_3 ions), the CH_3I^+ transient is measured simultaneously to the CH_3 transients corresponding to the different photodissociation channels. The CH_3I^+ transients are practically symmetric. Time zero is determined by fitting these transients using a single exponential decay function with a short time constant (usually below 50 fs) convoluted with the cross-correlation gaussian function (instrumental response function). Each set of CH_3 images measured at a given λ_{probe} yields a set of transients, each corresponding to a given photodissociation channel, for which time zero is precisely determined using the

in situ measured CH_3I^+ transient. The time zeros found using both methods are in a very good agreement within the experimental uncertainty.

IV. RESULTS AND DISCUSSION

A. Reaction times

Figure 2 depicts a summary of all the CH_3 transients measured for the different $\text{CH}_3(\nu_1, \nu_2) + \text{I}^*(^2P_{1/2})/\text{I}(^2P_{3/2})$ dissociation channels obtained in the femtosecond pump-probe velocity map imaging experiments described in the Experimental section. In addition, a representative CH_3I^+ transient measured *in situ* in order to determine time zero in each case is also shown. The corresponding clocking times are listed in Table II. Briefly, a reaction time around 100 fs is obtained for the dissociation channels in which spin-orbit excited $\text{I}^*(^2P_{1/2})$ is produced in correlation with vibrationless and $\nu_2 = 1, 2$ vibrationally excited CH_3 . In contrast, the clocking times for the different channels in which ground-state $\text{I}(^2P_{3/2})$ atoms are produced in correlation with vibrationless or vibrationally excited CH_3 fragments increases from about 60 fs for $\text{CH}_3(\nu = 0)$ to around 80 and 120 fs for CH_3 vibrationally excited into de umbrella mode, $\nu_2 = 1$ and $\nu_2 = 2$, respectively, and to more than 150 fs for CH_3 with one quantum of vibrational excitation into de ν_1 symmetric stretch mode. This increase of absolute reaction times for the $\text{I}(^2P_{3/2})$ channels as

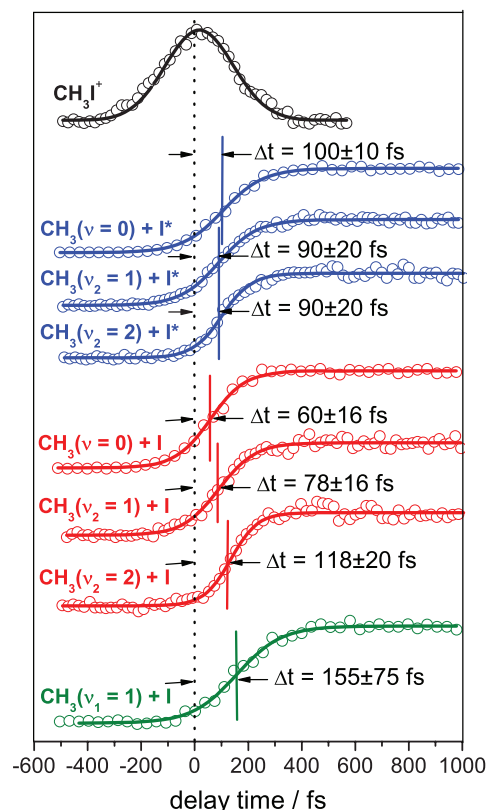


FIG. 2. CH_3 transients corresponding to the dissociation channels yielding $\text{CH}_3(\nu)$ in different vibrational states ($\nu = 0, \nu_1 = 1, \nu_2 = 1$ and $\nu_2 = 2$) in correlation with I and I^* . The reaction times (with statistical uncertainties) are indicated in each transient. A transient corresponding to the parent molecule CH_3I^+ defining the time zero is also depicted.

TABLE II. Experimental and calculated absolute and relative appearance times for the different CH₃(ν_1, ν_2) + I* (I) dissociation channels and I/I* branching ratios. The theoretical results are obtained applying different 4D and 3D models.

(ν_1, ν_2)	Expt.			
	(0, 0)	(0, 1)	(0, 2)	(1, 0)
I* channel, τ_1 (fs)	100 ± 10	90 ± 20	90 ± 20	
I channel, τ_2 (fs)	60 ± 16	78 ± 16	118 ± 20	155 ± 75
$\tau_1 - \tau_2$ (fs)	40	12	-28	
I/I* ratio	0.11 ± 0.02	0.45 ± 0.08	1.48 ± 0.03	
Present 4D model				
(ν_1, ν_2)	(0, 0)	(0, 1)	(0, 2)	(1, 0)
I* channel, τ_1 (fs)	95.5	97.1	100.9	
I channel, τ_2 (fs)	59.1	59.7	60.3	64.4
$\tau_1 - \tau_2$ (fs)	36.4	37.4	40.6	
I/I* ratio	0.06	2.0	127.0	
Present 3D model				
	$\nu_2 = 0$	$\nu_2 = 1$	$\nu_2 = 2$	
I* channel, τ_1 (fs)	95.6	97.1	99.8	
I channel, τ_2 (fs)	59.1	59.8	60.6	
$\tau_1 - \tau_2$ (fs)	36.5	37.3	39.2	
I/I* ratio	0.07	0.94	8.78	
Previous 3D model (Ref. 28)				
	$\nu_2 = 0$	$\nu_2 = 1$	$\nu_2 = 2$	
I* channel, τ_1 (fs)	113.8	115.6	118.5	
I channel, τ_2 (fs)	72.8	73.7	74.7	
$\tau_1 - \tau_2$ (fs)	41.0	41.9	43.8	
I/I* ratio	0.07	0.76	4.83	

vibrational excitation of the CH₃ fragment increases makes that the relative times between the channels yielding I*($^2P_{1/2}$) and I($^2P_{3/2}$) in correlation with the same vibrational state of the CH₃ fragment decrease substantially and even change sign (from 40 fs for vibrationless CH₃ to 12 and -28 fs for CH₃ with one quantum or two quanta of vibrational excitation into de ν_2 mode, respectively).

Time-dependent probability curves $P_{\nu_1, \nu_2}^{(i)}(t)$ of appearance of CH₃(ν_1, ν_2)+I*($^2P_{1/2}$) and CH₃(ν_1, ν_2)+I($^2P_{3/2}$) products have been calculated for the dissociation channels associated with $(\nu_1, \nu_2) = (0, 0), (0, 1), (0, 2),$ and $(1, 0)$ in the case of the 4D treatment, and with $\nu_2 = 0, 1,$ and 2 in the case of the 3D model. The time associated with half the asymptotic value of each calculated transient curve gives the theoretical dissociation reaction time or appearance time τ corresponding to each dissociation channel. The reaction times τ_1 and τ_2 associated with the I*($^2P_{1/2}$) and I($^2P_{3/2}$) dissociation channels, respectively, and the relative times $\tau_1 - \tau_2$ calculated with the different models are collected in Table II along with the experimental times.

Very good agreement is found between the experimental and theoretical 4D τ_1 times, as well as for the τ_2 time corresponding to the CH₃($\nu_1 = 0, \nu_2 = 0$)+I($^2P_{3/2}$) dissociation channel. Correspondingly, good agreement is also found between experiment and the 4D model for the $\tau_1 - \tau_2$ relative time of the $(\nu_1, \nu_2) = (0, 0)$ channel. However, agreement between experiment and the 4D model deteriorates rapidly as excitation of the CH₃(ν_1, ν_2) increases either in the umbrella or the symmetric stretch mode. The trend observed experimentally is that with increasing vibrational excitation of CH₃(ν_1, ν_2), dissociation through the I($^2P_{3/2}$)

channel becomes increasingly slower, being even slower than dissociation through the I*($^2P_{1/2}$) channel despite that for this latter channel there is ~1 eV less energy available for the fragments. The trend found theoretically for the I($^2P_{3/2}$) channels is also an increase of the reaction time with increasing vibrational excitation of the CH₃(ν_1, ν_2) fragment. However, the increase of the calculated τ_2 times is very small compared to the experimental one. The increase found theoretically is consistent with the small decrease of energy available to the fragments due to the increasing vibrational excitation of CH₃(ν_1, ν_2). It is noted that the trend of a small increase of τ_2 displayed by the 4D results is the same as the trend obtained with the 3D model (see Ref. 28 and present results).

Interestingly, Table II shows that the reaction times obtained with the current 3D model are practically the same as the 4D times. Thus, the level of agreement between the current 3D times and the experimental ones is the same as that of the 4D reaction times. The improvement in the description of the experimental reaction times by the present 4D and 3D models with respect to the previous 3D treatment²⁸ is due to the averaging of the calculated probabilities over the spectral bandwidth of the pump laser pulse carried out in the present models. Actually, all the energies contained in the pump pulse bandwidth contribute to the CH₃ time-dependent transients detected experimentally, and therefore to the experimental appearance times, and this effect should be considered in the simulations. The present improved agreement between the theoretical and experimental reaction times indicates that including in the theoretical models the effect of the pump pulse bandwidth (not considered in the previous 3D simulations), along with the effect of the probe pulse

bandwidth indeed provides a more realistic description of the experimental conditions.

The results of Table II involve a few interesting implications. First, the nearly identical reaction times obtained with the current 4D and 3D models imply that the role played by the symmetric stretch mode in the dynamics is rather small, being essentially an spectator mode. Practically, all the system remains in the ground vibrational state $\nu_1 = 0$ during the photodissociation process, and only a very small fraction of the wave packet produces excited $\text{CH}_3(\nu_1 = 1, \nu_2 = 0)$ fragments through the $\text{I}(^2P_{3/2})$ dissociation channel, being this fraction much smaller than that found experimentally.²⁸ The small probability of $\text{CH}_3(\nu_1 = 1, \nu_2 = 0)$ products predicted theoretically can be due to some deficiencies of the *ab initio* potentials and the nonadiabatic coupling used in the 4D model. In this sense, it is noted that the 9D MCTDH description of the CH_3I photodissociation also predicts a negligible excitation of the CH_3 symmetric stretch mode in the $\text{I}(^2P_{3/2})$ channel.¹⁵ This result seems to support that the origin of the discrepancy between the experimental and theoretical fraction of $\text{CH}_3(\nu_1 = 1, \nu_2 = 0)$ fragments lies on deficiencies of the potential surfaces rather than on the reduced-dimensionality nature of the 4D model. We also note that the description of the symmetric stretch mode by a set of basis functions in the 4D model and by fixing the C–H distances at their equilibrium value in the 3D model, seems to make no difference regarding the results of a rather global property as the reaction time.

Second, the 3D model appears to perform extremely well as compared to the 4D approach despite that in the 3D treatment the description of the umbrella angular mode is approximated by a radial coordinate, and that the expression of the kinetic energy operator of the Hamiltonian in the 3D model is simplified²⁸ compared to that of Eq. (1). This implication is very important since the 4D model is by far much more demanding computationally than the 3D one. On the other hand, this result assesses the quality of recent wave packet calculations reported on the photodissociation of CD_3I using the 3D model.³¹

Third, the discrepancy between experiment and theory regarding the increase of the τ_2 reaction times with increasing vibrational excitation of the CH_3 fragment still remains in the 4D description. This is so despite that an additional mode, the symmetric stretch one, is included with respect to the 3D model, and that all four modes and their corresponding couplings are correctly described in the 4D Hamiltonian used. In Ref. 28, it was suggested that the discrepancy between theory and experiment could be due to the absence of a correct description in the 3D model of vibrational couplings between the umbrella mode and other modes, like the symmetric stretch mode. These couplings would become more important in the photodissociation dynamics with increasing vibrational excitation of the CH_3 fragment. The present results rule out that possibility, since now the couplings are correctly included in the model, but the discrepancy remains.

The four modes considered in the 4D model are expected to be the most relevant ones for the CH_3I dissociation dynamics, and it is unlikely that the discrepancy is due to neglecting

one or more of the remaining five modes. The possibility that the asymmetric stretch mode of the CH_3 group (instead of the symmetric stretch mode) and its couplings with the umbrella mode may play an important role in the behavior of the τ_2 reaction times cannot be discarded at present. However, the similar results provided by the 5D and 9D MCTDH descriptions¹⁵ do not support strongly this possibility. On the other hand, it is intriguing that the theoretical description of the reaction times (either 4D or 3D) is good for the $\text{I}^*(^2P_{1/2})$ dissociation channels, even with vibrational excitation of the CH_3 fragment, while it fails for the $\text{I}(^2P_{3/2})$ dissociation channels when vibrational excitation of the CH_3 product takes place. This result would be consistent with deficiencies in the *ab initio* potentials, and in particular in the 1Q_1 surface, which is unable to reproduce the dependence found experimentally on the CH_3 umbrella mode excitation.

Another possibility is that the discrepancy is not due to poor description of the dynamics by the models, but instead to an effect of the experimental detection of the fragments that treats differently the $\text{I}^*(^2P_{1/2})$ and the $\text{I}(^2P_{3/2})$ channels, and which is not considered in the theoretical models. In the present experiments, the CH_3 fragment in different vibrational states ($\nu = 0, \nu_2 = 1$ and $\nu_2 = 2$) is detected by a 2+1 REMPI process, in which two probe photons are first absorbed resonantly to the vibrational states of the intermediate $3p_z$ Rydberg electronic state and then a third photon is absorbed up to the ionization continuum. In the simulation of the observation window described in Sec. II C, only the shapes of the adiabatic valence 3Q_0 and 1Q_1 potential energy curves and the bandwidth of the probe pulse are considered. This implies to assume that the Rydberg state potential energy curves are flat, i.e. independent of the C–I distance. However, it is evident that the Rydberg potential energy curves will show also a strong dependence on the C–I distance. The adiabatic potential energy curves associated with the valence 3Q_0 and 1Q_1 electronic states correlating with $\text{CH}_3(\nu)+\text{I}^*$ used in the simulation of the observation window are rather parallel to each other (see Fig. 12 in Ref. 28). If the adiabatic potential energy curves corresponding to the Rydberg states are not so parallel, then the resonance that enhances the multiphoton ionization could be reached at different C–I distances and thus different opening windows and reaction times could be found for each CH_3 vibrational state.

In order to check for this possibility, we have carried out *ab initio* calculations of the electronic states involved in the multiphoton detection scheme used for the detection of the different vibrational states of the $3p_z$ Rydberg electronic state of the CH_3 fragment. Two dimensional potential energy surfaces along the dissociation and umbrella coordinates were calculated for this electronic state. The nuclear Hamiltonian was described considering a pseudo-triatomic molecule and the nuclear eigenfunctions for the umbrella mode were obtained at every internuclear C–I distance using the Fourier Grid Hamiltonian method.³⁶ The electronic energy was calculated using perturbation theory in its multistate version (MS-CASPT2).⁴⁶ The underlying state average complete active space (SA-CASSCF) (Ref. 47) scheme was evaluated with the ANO-RCC basis set⁴⁸ contracted to a QZP and the

active space was constructed with 6 electrons in 8 orbitals, including the 5 *p* orbitals of the I-atom and the lone pair, together with the *s* and *p* Rydberg orbitals in the CH₃ fragment. In order to maintain the degeneration, 16 singlets and 15 triplets were included in the State Average wavefunction and the Douglas-Kroll Hamiltonian and the spin-orbit AMFI approximations were employed to take into account relativistic effects.^{49,50} These calculations were performed with the MOLCAS package.⁵¹

The results obtained from these *ab initio* calculations indicate that the corresponding adiabatic potential energy curves for the 3*p_z* Rydberg states involved in the probing step of the CH₃(*v*) fragments for both the I and I* channel are also rather parallel. Thus, there is no change in the opening of the observation window for the different vibrational states of the CH₃ fragment due to the intermediate 3*p_z* Rydberg state and this cannot justify the observed reaction times. However, it must be considered that the present *ab initio* calculations are not taking into account the effect of the 3*s* Rydberg electronic state, which is very important in the enhancement of the two-photon absorption to the 3*p_z* state. In addition, due to the complexity of the system, the Rydberg states of the iodine atom have not been included in the calculations and the possible interaction of the 3*p_z* of the CH₃ and the I-atom

Rydberg state could modify the potential energy surfaces. In any case, we rely on these results and believe that the explanation for the different reaction times cannot be found in the probing step.

In Table II, the experimental and theoretical I/I* branching ratios are also shown for the different dissociation channels. For the (*v*₁, *v*₂) = (0, 0) dissociation channel, the present and previous theoretical predictions for the I/I* ratio are similar, and they agree reasonably well with the corresponding experimental ratio. As the umbrella mode of CH₃ becomes excited the theoretical and experimental I/I* ratios become increasingly different, as it happens with the τ_2 reaction times. For *v*₂ = 1 and 2, the I/I* ratios obtained with the current 4D and 3D models are larger than in the previous 3D simulations,²⁸ specially in the case of the 4D model. The I/I* ratio as a function of *v*₂ is strongly dependent on the CH₃ product vibrational distributions produced in the I*(²*P*_{1/2}) and I(²*P*_{3/2}) dissociation channels. As we shall see below, the current 4D and 3D models predict colder CH₃ vibrational distributions in the I*(²*P*_{1/2}) channel than the previous 3D approach,²⁸ specially in the 4D case where the *v*₂ = 2 population practically vanishes. This explains the significant increase of the I/I* ratio predicted by the present 4D and 3D models for *v*₂ = 1 and 2.

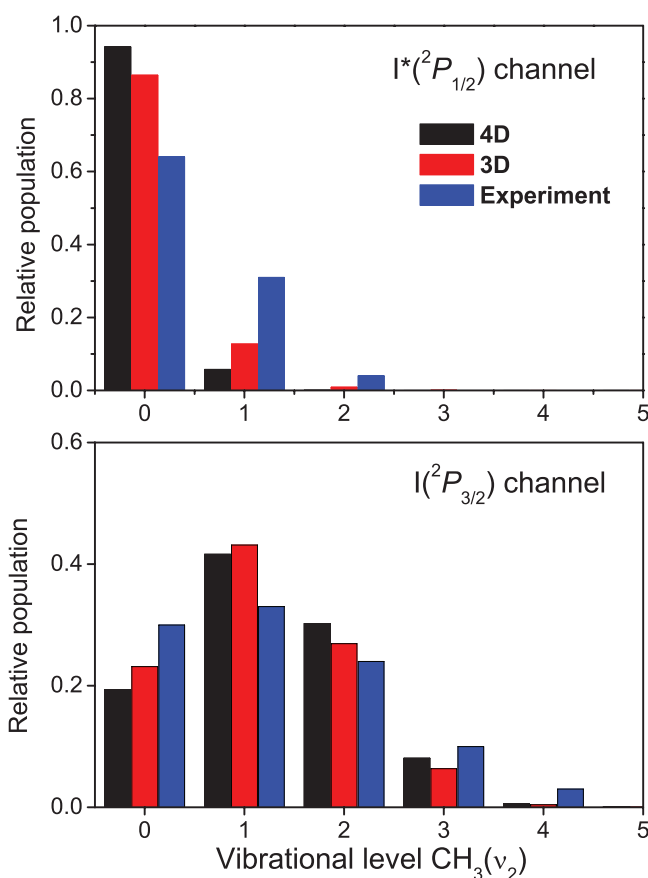


FIG. 3. Calculated vibrational distributions of the CH₃(*v*₁ = 0, *v*₂) fragment produced through the I* channel (upper panel) and the I channel (lower panel) using the 4D and the 3D models. Experimental distributions measured for 266 nm excitation taken from Ref. 23 are also displayed in the figure for comparison.

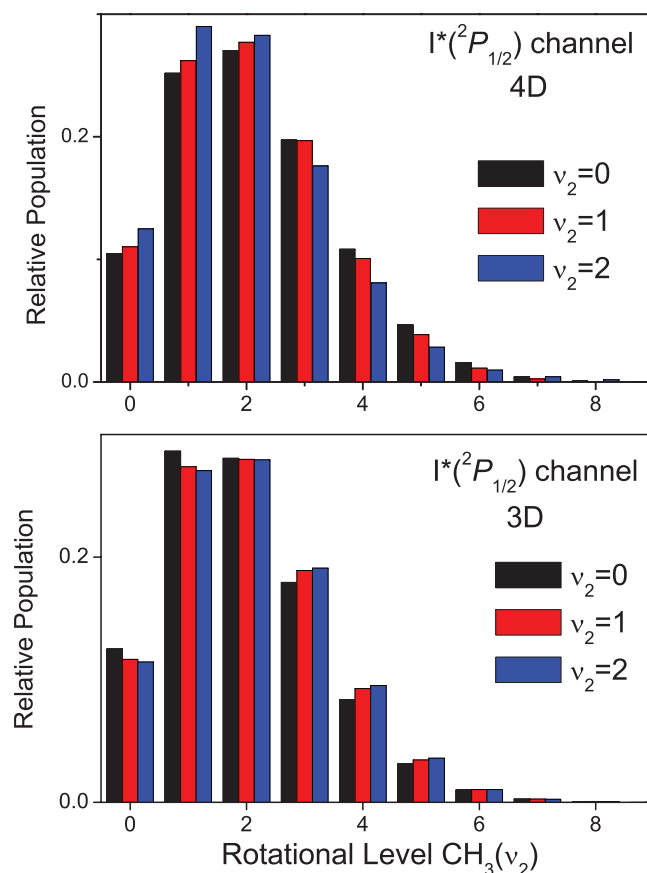


FIG. 4. Calculated rotational distributions of the CH₃(*v*₁ = 0, *v*₂) fragment produced through the I* channel for the first three vibrational states *v*₂ = 0, *v*₂ = 1, and *v*₂ = 2, using the 4D (upper panel) and the 3D (lower panel) models.

B. Product fragment state distributions

In addition to reaction times and I/I^* branching ratios, it is interesting to compare the predictions of the 4D and 3D models for less global properties such as product state distributions like vibrational, rotational, and translational energy distributions of the CH_3 fragment. Vibrational and rotational distributions of the CH_3 product have been calculated for the asymptotic value $R_c = 12.99 a_0$ for the $I^*(^2P_{1/2})$ and $I(^2P_{3/2})$ dissociation channels. In the calculation of these distributions, averaging over the spectral bandwidth of the pump laser pulse has been carried out. It is noted, however, that it has been recently shown that the pump pulse spectral bandwidth affects very little the shape of the CH_3 fragment vibrational and rotational distributions.³³

Vibrational distributions of the CH_3 fragment obtained with the 4D and 3D models for the $I^*(^2P_{1/2})$ and $I(^2P_{3/2})$ dissociation channels are displayed in Fig. 3 along with experimental distributions measured for 266 nm excitation.²³ The two theoretical distributions corresponding to the $I^*(^2P_{1/2})$ dissociation channel are significantly colder than the experimental one. Agreement between the theoretical and experimental distributions is better in the case of the $I(^2P_{3/2})$ dissociation channel, although the theoretical distributions are still somewhat hotter. The distributions obtained with the 4D and 3D models are found to be quite similar, particularly for the $I(^2P_{3/2})$ dissociation channel. We note that the CH_3 vibrational distributions are properties less global and less averaged than the

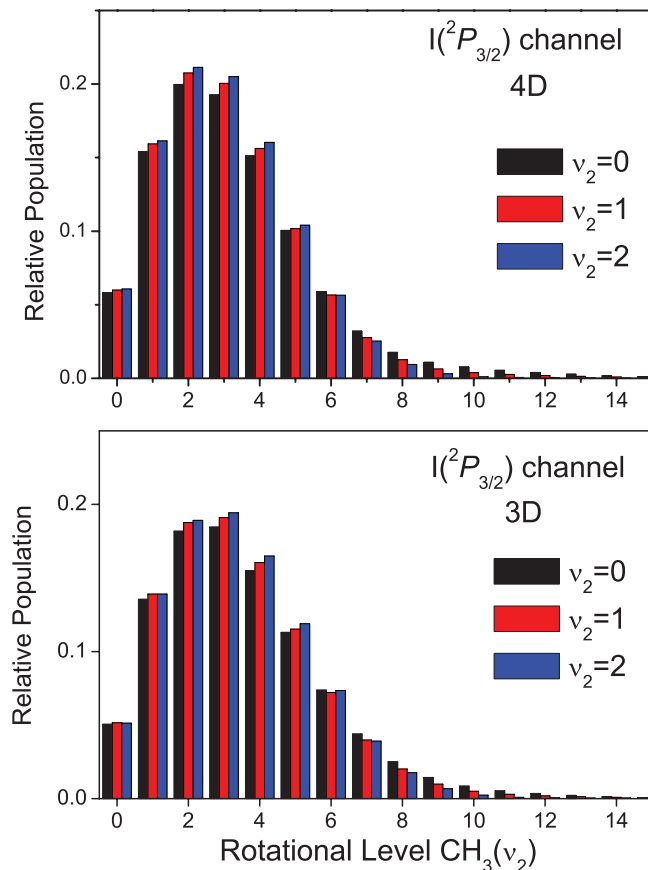


FIG. 5. Same as Fig. 4 but for the I dissociation channel.

reaction times analyzed above, but still the outcome produced by the 4D and 3D models for these distributions is very similar. On the other hand, as commented above, in the case of the $I^*(^2P_{1/2})$ channel distributions, the $v_2 = 1$ and 2 populations obtained with the 4D model are smaller (the $v_2 = 2$ population is practically zero) than those of the 3D model, which explain the larger I/I^* ratios of the 4D results shown in Table II.

Rotational distributions of the $\text{CH}_3(v_1 = 0, v_2)$ fragment have been calculated for the I^* and I channels and $v_2 = 0, 1$, and 2 using the 4D and 3D models, and they are compared in Figs. 4 and 5. Rotational distributions are less averaged and more sensitive magnitudes than reaction times and vibrational distributions, so in principle more differences between the two models are expected in this case. The differences found, however, are essentially quantitative, and the 4D and 3D distributions display a very similar shape for all of the dissociation channels.

Differences between the two models are somewhat larger for the I^* channel. Indeed, in this case the 4D model predicts that with increasing v_2 excitation the rotational distributions

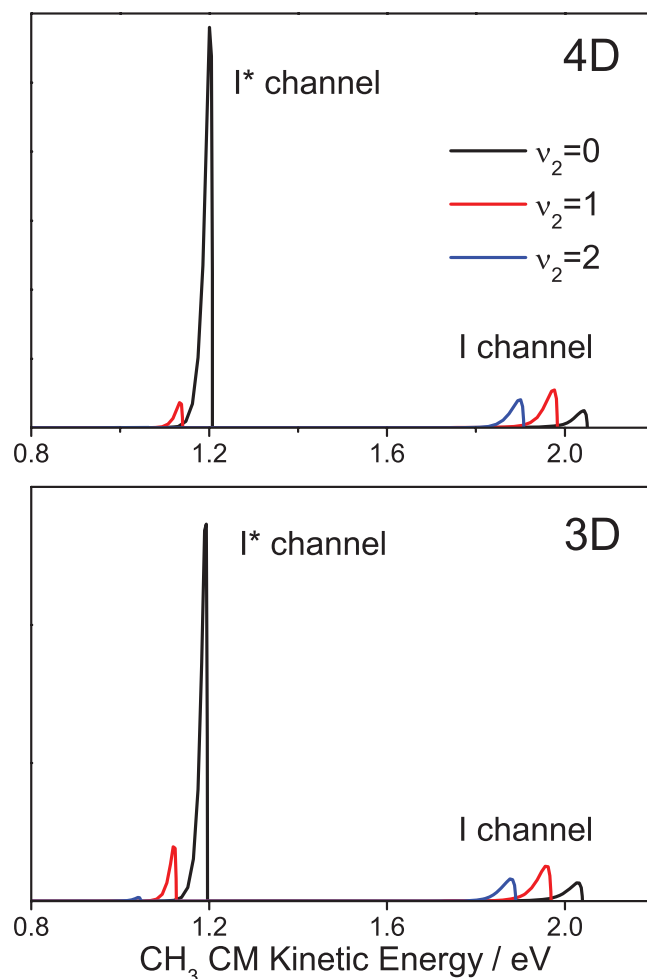


FIG. 6. Calculated translational energy distributions of the $\text{CH}_3(v_1 = 0, v_2) + I^*(I)$ fragments for the first three vibrational states $v_2 = 0, v_2 = 1$, and $v_2 = 2$ vs the translational energy of the CH_3 center-of-mass, using the 4D (upper panel) and the 3D (lower panel) model.

become increasingly colder, while the 3D model predicts the opposite trend, namely that the distributions become hotter. The prediction of the 4D model appears to be more correct, since increasing excitation in the umbrella mode implies a decreasing amount of energy available for the fragments.

The differences between the 4D and 3D distributions in the I channel (Fig. 5) are smaller than for the I* channel, similarly as in the case of the vibrational distributions of Fig. 3. The I* channel distributions seem to be somewhat more sensitive to the use of a more correct 4D description of the dynamics. In the I channel both the 4D and the 3D distributions predict the same trend that with increasing vibrational excitation the distributions become colder. The small quantitative differences between the 4D and 3D results cause that the maximum of the 4D distributions occurs at $j = 2$, while the 3D distributions peak at $j = 3$.

Translational energy distributions of the CH₃($\nu_1 = 0, \nu_2$) fragment with $\nu_2 = 0, 1$, and 2 were calculated for the I* and I channels with the 4D and 3D models (see Fig. 6). Again small differences are found between the 4D and 3D results. Particularly similar are the distributions of the I channel, indicating once again that this channel is affected rather little by changing from a 3D to a 4D dynamical description. For the I* dissociation channel, the $\nu_2 = 0$ distributions are very similar in the 4D and 3D results, and the differences are located mainly in the $\nu_2 = 1$ and 2 distributions, which are substantially less intense in the 4D description.

V. CONCLUSIONS

The CH₃I photodissociation dynamics has been studied using a wave packet model including four degrees of freedom, namely the C–I dissociation coordinate, the I–CH₃ bending mode, the CH₃ umbrella mode, and the C–H symmetric stretch mode. The theoretical reaction times are compared with those obtained in femtosecond velocity map imaging experiments. The model reproduces very well the experimental reaction times for the CH₃(ν_1, ν_2)+I*(²P_{1/2}) dissociation channels with $\nu_1 = 0$ and $\nu_2 = 0, 1, 2$, and also for the channel CH₃($\nu_1 = 0, \nu_2 = 0$)+I(²P_{3/2}). The model fails, however, to predict the experimental clocking times for the CH₃(ν_1, ν_2)+I(²P_{3/2}) channels with $(\nu_1, \nu_2) = (0, 1), (0, 2),$ and $(1, 0)$, i.e., when the CH₃ fragment produced along with spin-orbit ground state I atoms is vibrationally excited. The reaction times and product fragment state distributions obtained with the 4D model are compared with those calculated with a similar 3D wave packet model that neglects the CH₃ symmetric stretch mode. Very small differences are found between the results of the 4D and 3D models, also regarding the discrepancy with the experimental reaction times for the I dissociation channel. This indicates that the contribution of the CH₃ symmetric stretch mode to the theoretical description of the dynamics is rather irrelevant and therefore unable to improve the theoretical prediction of the I channel reaction times. The 2+1 REMPI probing process of the CH₃ fragment has been ruled out as the reason for the increasing reaction times as the vibrational excitation of the CH₃ fragment increases for the I channel through *ab initio* calculations of the intermediate 3p_z Rydberg state of

the CH₃ fragment as a function of the C–I distance. At this point, no theoretical explanation has been found for the experimental reaction times for the I channel yielding vibrationally excited CH₃. Deficiencies of the *ab initio* potentials used, and in particular of the ¹Q₁ electronic surface, could be responsible for the failure of the models in reproducing the vibrational dependence of the reaction times observed experimentally.

ACKNOWLEDGMENTS

J.D. gratefully acknowledges financial support through a Unidad Asociada-CSIC fellowship. J.G.-V. is financially supported by a Juan de la Cierva postdoctoral contract from the Spanish Ministry of Science and Innovation (MICINN). This work has been financed by MICINN through Grants CTQ2008-02578/BQU, FIS2010-18132, and Consolider program “Science and Applications of Ultrafast Ultraintense Lasers” No. CSD2007-00013. This research has been performed within the Unidad Asociada “Química Física Molecular” between Departamento de Química Física I of Complutense University Madrid (UCM) and CSIC. The facilities provided by the Centro de Asistencia a la Investigación de Espectroscopia Multifotónica y de Femtosegundo (UCM) are gratefully acknowledged. The Centro de Supercomputación de Galicia (CESGA) is acknowledged for the use of its resources.

- ¹A. Gedanken and M. D. Rowe, *Chem. Phys. Lett.* **34**, 39 (1975).
- ²M. Shapiro and R. Bersohn, *J. Chem. Phys.* **73**, 3810 (1980).
- ³M. Shapiro, *J. Phys. Chem.* **90**, 3644 (1986).
- ⁴D. W. Chandler and P. L. Houston, *J. Chem. Phys.* **87**, 1445 (1987).
- ⁵R. O. Loo, H.-P. Haerri, G. E. Hall, and P. L. Houston, *J. Chem. Phys.* **90**, 4222 (1989).
- ⁶I. Powis and J. F. Black, *J. Phys. Chem.* **93**, 2461 (1989).
- ⁷D. W. Chandler, J. W. Thoman, Jr, M. H.M. Janssen, and D. H. Parker, *Chem. Phys. Lett.* **156**, 151 (1989).
- ⁸D. W. Chandler, M. H.M. Janssen, S. Stolte, R. N. Strickland, J. W. Thoman, and D. H. Parker, *J. Phys. Chem.* **94**, 4893 (1990).
- ⁹H. Guo and G. C. Schatz, *J. Chem. Phys.* **93**, 393 (1990).
- ¹⁰Y. Amatatsu, K. Morokuma, and S. Yabushita, *J. Chem. Phys.* **94**, 4858 (1991).
- ¹¹H. Guo, K. Q. Lao, G. C. Schatz, and A. D. Hammerich, *J. Chem. Phys.* **94**, 6562 (1991).
- ¹²H. Guo, *J. Chem. Phys.* **96**, 6629 (1992).
- ¹³U. Manthe and A. D. Hammerich, *Chem. Phys. Lett.* **211**, 7 (1993).
- ¹⁴A. D. Hammerich, U. Manthe, R. Kosloff, H.-D. Meyer, and L. S. Cederbaum, *J. Chem. Phys.* **101**, 5623 (1994).
- ¹⁵C. R. Evenhuis and U. Manthe, *J. Phys. Chem. A* **115**, 5992 (2011).
- ¹⁶B. R. Johnson, C. Kittrell, P. B. Kelly, and J. L. Kinsey, *J. Phys. Chem.* **100**, 7743 (1996).
- ¹⁷Y. Amatatsu, S. Yabushita, and K. Morokuma, *J. Chem. Phys.* **104**, 9783 (1996).
- ¹⁸A. T. J. B. Eppink and D. H. Parker, *J. Chem. Phys.* **109**, 4758 (1998).
- ¹⁹A. T. J. B. Eppink and D. H. Parker, *J. Chem. Phys.* **110**, 832 (1999).
- ²⁰D. Zhong and A. H. Zewail, *J. Phys. Chem. A* **102**, 4031 (1998).
- ²¹D. Xie, H. Guo, Y. Amatatsu, and R. Kosloff, *J. Phys. Chem. A* **104**, 1009 (2000).
- ²²A. J. van den Brom, M. L. Lipciuc, M. H.M. Janssen, *Chem. Phys. Lett.* **368**, 324 (2003).
- ²³G. Li, H. J. Hwang, and H. C. Jung, *Rev. Sci. Instrum.* **76**, 023105 (2005).
- ²⁴G. Li and H. J. Hwang, *J. Chem. Phys.* **124**, 244306 (2006).
- ²⁵A. B. Alekseyev, H.-P. Liebermann, R. J. Buenker, and S. N. Yurchenko, *J. Chem. Phys.* **126**, 234102 (2007).

- ²⁶A. B. Alekseyev, H.-P. Liebermann, and R. J. Buenker, *J. Chem. Phys.* **126**, 234103 (2007).
- ²⁷R. de Nalda, J. G. Izquierdo, J. Durá, and L. Bañares, *J. Chem. Phys.* **126**, 021101 (2007).
- ²⁸R. de Nalda, J. Durá, A. García-Vela, J. G. Izquierdo, J. González-Vázquez, and L. Bañares, *J. Chem. Phys.* **128**, 244309 (2008).
- ²⁹J. Durá, R. de Nalda, J. Alvarez, J. G. Izquierdo, G. A. Amaral, L. Bañares, *ChemPhysChem* **9**, 1245 (2008).
- ³⁰J. Durá, R. de Nalda, G. A. Amaral, L. Bañares, *J. Chem. Phys.* **131**, 134311 (2009).
- ³¹A. García-Vela and L. Bañares, *Chem. Phys. Lett.* **477**, 271 (2009).
- ³²L. Rubio-Lago, A. García-Vela, A. Arregui, G. A. Amaral, and L. Bañares, *J. Chem. Phys.* **131**, 174309 (2009).
- ³³A. García-Vela and L. Bañares, *Phys. Chem. Chem. Phys.* **13**, 2228 (2011).
- ³⁴G. Gitzinger, M. E. Corrales, V. Loriot, G. A. Amaral, R. de Nalda, and L. Bañares, *J. Chem. Phys.* **132**, 234313 (2010).
- ³⁵N. Thiré, R. Cireasa, V. Blanchet, and S. T. Pratt, *Phys. Chem. Chem. Phys.* **12**, 15644 (2010).
- ³⁶C. C. Marston and G. G. Balint-Kurti, *J. Chem. Phys.* **91**, 3571 (1989).
- ³⁷C. Yamada, E. Hirota, and K. Kawaguchi, *J. Chem. Phys.* **75**, 5256 (1981).
- ³⁸H. W. Hermann and S. R. Leone, *J. Chem. Phys.* **76**, 4766 (1982).
- ³⁹N. E. Triggs, M. Zahedi, J. W. Nibler, P. DeBarber, and J. J. Valentini, *J. Chem. Phys.* **96**, 1822 (1992).
- ⁴⁰P. B. Kelly and S. G. Westre, *Chem. Phys. Lett.* **151**, 253 (1988).
- ⁴¹G. G. Balint-Kurti, R. N. Dixon, and C. C. Marston, *J. Chem. Soc. Faraday Trans.* **86**, 1741 (1990).
- ⁴²G. G. Balint-Kurti, R. N. Dixon, and C. C. Marston, *Int. Rev. Phys. Chem.* **11**, 317 (1992).
- ⁴³Our design is based on the original design by Professor D. Gerlich (<http://www.tu-chemnitz.de/physik/ION/Technology/PiezoValve/index.html>).
- ⁴⁴A. T. J. B. Eppink and D. H. Parker, *Rev. Sci. Instrum.* **68**, 3477 (1997).
- ⁴⁵G. A. Garcia, L. Nahon, and I. Powis, *Rev. Sci. Instrum.* **75**, 4989 (2004).
- ⁴⁶J. Finley, P.-A. Malmqvist, B. O. Roos, and L. Serrano-Andrés, *Chem. Phys. Lett.* **288**, 299 (1998).
- ⁴⁷B. O. Roos, *Chemical Physics* **69**, 399 (1987).
- ⁴⁸B. O. Roos, R. Lindh, P.-A. Malmqvist, V. Veryazov, and P.-O. Widmark, *J. Phys. Chem. A* **108**, 2851 (2004).
- ⁴⁹M. Reiher and A. Wolf, *J. Chem. Phys.* **121**, 2037 (2004).
- ⁵⁰M. Reiher and A. Wolf, *J. Chem. Phys.* **121**, 10945 (2004).
- ⁵¹G. Karlström, R. Lindh, P.-A. Malmqvist, B. O. Ross, U. Ryde, U. Veryazov, P.-O. Widmark, M. Cossi, B. Schimmelpfennig, P. Neogady, and L. Seijo, *Comput. Mater. Sci.* **28**, 222 (2003).